# Metal-Semiconductor-Metal Photodetectors on a GeSn-on-Insulator Platform for 2 μm Applications

Bongkwon Son [ID], Yiding Lin [ID], Kwang Hong Lee, Joe Margetis, David Kohen, John Tolle, and Chuan Seng Tan [ID], *Fellow, IEEE*

*Abstract*—In this work, the metal-semiconductor-metal photodetectors were demonstrated on the $Ge_{0.91}Sn_{0.09}$-on-insulator (GeSnOI) platform. The responsivity was 0.24 and 0.06 A/W at wavelengths of 1,600 and 2,003 nm, respectively. Through a systematic study, it is revealed that the photodetectors can potentially detect wavelength beyond 2,200 nm. The dark current density was measured to be 4.6 $A/cm^2$ for GeSnOI waveguide-shaped photodetectors. The 3 dB bandwidth was observed to be 1.26 and 0.81 GHz at 1,550 and 2,000 nm wavelengths, respectively. This work opens up an opportunity for low-cost 2 μm wavelength photodetection on the GeSn/Ge interface-free GeSnOI platform.

*Index Terms*—Germanium-tin alloys, germanium-tin on insulator, metal-semiconductor-metal photodetector.

## I. INTRODUCTION

GERMANIUM-tin (GeSn) alloys have been promising for silicon (Si)-based photonic-integrated circuits (PICs), leading to the technological advances in 5G, Internet of Things, fiber-optic telecommunication, and Light Detection and Ranging operating in the near- and mid-infrared (MIR) range. Ge itself is a quasi-direct bandgap material with the direct bandgap at the wavelength of 1550 nm. Alloying of Ge with Sn allows a shrinkage of the Ge bandgap, extending the photodetection range beyond 2000 nm wavelength [1]. Especially including hollow-core fiber optics, sensing, and imaging applications, the 2000 nm photodetection is desirable, but III-V material systems have received much attention for that wavelength [2], [3].

However, Si-based photonic components are needed due to the compatibility of the complementary metal-oxide-semiconductor (CMOS) process, aiming for high volume and cost-effective integration [4].

Since GeSn photodetectors with the Sn content of 3% extended the cut-off wavelength up to 1800 nm [5], numerous efforts have been made for high-performance GeSn photodetectors. The main interests of the 2000 nm photodetection were realized for GeSn photodetectors with the Sn content of 6% [6]. After that, the optical responsivity was enhanced by employing the photon-trapping hole structures [7], on-insulator platforms [8], and lateral light injection using waveguide photodetectors [9]. A photodetector integrated on waveguides are promising to vanish the trade-off between optical responsivity and 3dB-bandwidth by separating the paths of photon absorption and carrier transmission [10].

Although the theoretical calculation expects that the defect-free GeSn photodetectors are comparable with the existing commercial III-V photodetectors [11], the reported GeSn photodetectors have suffered from the high leakage current and low optical responsivity. The prominent leakage current is originated from the high density of dislocations/defects generated during the GeSn growth due to low solubility of Sn in Ge, low-temperature growth, and large lattice mismatch [12]. In particular, many dislocations are formed at the GeSn/Ge interface [13], degrading the dark current density and external quantum efficiency for photodetectors [14], [15]. Therefore, recent GeSn photonic components have been developed in managing the defective GeSn layers, achieving excellent performances of optical devices [16], [17].

Recently, GeSn-on-insulator (GeSnOI) platforms via direct wafer bonding (DWB) and layer transfer techniques have been reported [18]. The demonstrated GeSnOI platform is a promising pathway for monolithic integration on Si. In addition, the platform benefits from the removal of the defective GeSn/Ge interface that can potentially reduce the dark leakage current for photodetectors. In this work, metal-semiconductor-metal (MSM) photodetectors have been demonstrated on the GeSnOI platform. Systematic characterization demonstrates the advantage of the GeSnOI substrate without GeSn/Ge and GeSn/Si interfaces. The waveguide-shaped MSM photodetectors on the GeSnOI platform display the dark current density of 4.6 $A/cm^2$. Based on the photoluminescence (PL) measurement, the cut-off wavelength for photodetectors is estimated to be beyond 2200 nm. The optical response measurement was performed at
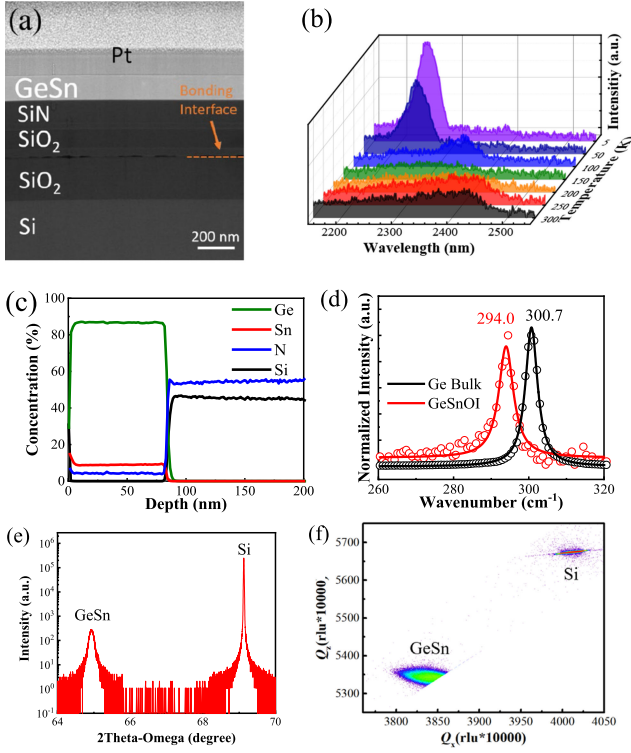
Fig. 1. (a) The cross-view TEM image for the GeSnOI substrate. (b) PL measurements as a function of wavelength in temperature ranging from 5 to 300 K. (c) SIMS content profiles for GeSnOI substrate. (d) Raman spectra for the GeSnOI platform and Ge bulk. (e) HRXRD curves in (004) direction for the GeSnOI platform. (f) RSM image of the GeSnOI platform in (224) direction.

wavelengths from 1600 to ∼2000 nm under normal incidence illumination. The responsivity was obtained to be 0.24 and 0.06 A/W at the wavelength of 1600 and 2003 nm, respectively. This work provides the great potential of MSM photodetectors on the GeSnOI platform with the GeSn/Ge or GeSn/Si interface-free, aiming for high sensitivity and high-speed optical communication.

## II. FABRICATION AND CHARACTERIZATION OF GESNOI MSM PHOTODETECTORS

GeSn/Ge layers were grown on a 200-mm Si substrate through a reduced pressure chemical vapor deposition (RPCVD) reactor. The silicon nitride (SiN) and silicon dioxide (SiO$_2$) layers were adopted for the insulator substrate. The SiN insulator allows for the optical-transparent window beyond 3.8 μm [19]. DWB and layer transfer techniques were implemented to form the GeSnOI stack at the maximum temperature of 300°C. The overall process sequence is shown in Ref [18]. It should be noted that the Si and Ge layers can be etched selectively by tetramethylammonium hydroxide solution [18] and dry etching in a CF$_4$ RF plasma, respectively [19].

A transmission electron microscopy (TEM) image of the bonded GeSnOI is illustrated in Fig. 1(a). The GeSn thickness is 133 nm. The SiN and SiO$_2$ layers with thicknesses of 120 and 400 nm, respectively, were formed underneath the GeSn layer after the DWB and layer transfer processes. The PL experiment
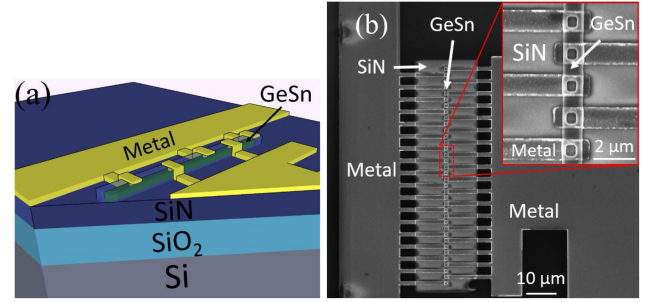


Fig. 2. (a) The A 3D schematic image of the GeSnOI MSM photodetector. (b) the planar view of the SEM image of GeSnOI MSM photodetector. The inset in Fig. 2(b) displays the zoom-in image of the GeSn photodetector.

was conducted to verify the interband emission via band-edges in the temperature range of 5 to 300 K in Fig. 2(b). At 5 K, the PL peak appears at 2242 nm wavelength, and the broad emission was observed at 2400 nm wavelength at 300 K [20]. The PL peak at the wavelength of 2242 nm at 5 K is attributed to the direct bandgap emission, implying that the cut-off wavelength is beyond 2000 nm at 5 K, and it extends further when the temperature increases. Fig. 1(c) represents the element profiles via Secondary-ion mass spectrometry (SIMS) analysis. The Sn content of 8.9% was uniformly distributed in the GeSn layer in the wafer scale. Raman spectroscopy was conducted using the laser with 532 nm of wavelength in Fig. 1(d). The Raman peak shifts from 300.7 to 294.0 cm$^{-1}$ for GeSnOI. The peak shift dependence can be explained by the changes in Sn content and strain information as follows [21],

$$\Delta\omega = -88x + 521\varepsilon_{\text{Strain}}, \tag{1}$$

where $\Delta\omega$, $x$, and $\varepsilon_{\text{Strain}}$ are the Raman spectral shift, Sn composition, and strain, respectively. Given Sn content in SIMS analysis, the strain was extracted to be -0.22%. This value is relaxed in comparison with as-grown GeSn layers, meaning that the GeSnOI platform is beneficial to the strain-relaxation of epitaxial GeSn layers. High-resolution X-ray diffraction (HRXRD) and reciprocal space map (RSM) for the GeSnOI platform are performed in Fig. 1(e) and (f), respectively. Fig. 1(e) shows Si and the GeSn layer peaks, indicating the successful realization of the GeSn/Ge interface-free GeSnOI platform. The Sn content and its strain value can be estimated based on RSM images in Fig. 1(f) [22], [23]. The estimated Sn content and strain are 9.2% and -0.22%, respectively, matching the ones obtained via SIMS analysis and Raman spectroscopy, respectively.

The MSM photodetectors were then demonstrated using the intrinsic GeSn on the insulator platform. The chlorine (Cl$_2$)-based reactive ion etching (RIE) process defined the waveguide shape with 1 μm width and the lengths of 12, 36, 72, and 108 μm. After that, the 1 nm thick Al$_2$O$_3$ layer was deposited via the atomic layer deposition (ALD) technique to alleviate the Fermi pinning effect and produce the etch stop layer for the metal-contact holes [24]. Subsequently, the SiN layer was covered via Plasma Enhanced Chemical Vapor Deposition (PECVD). The sulfur hexafluoride (SF$_6$)-based RIE process was implemented to open the metal-contact holes. The sputtering of
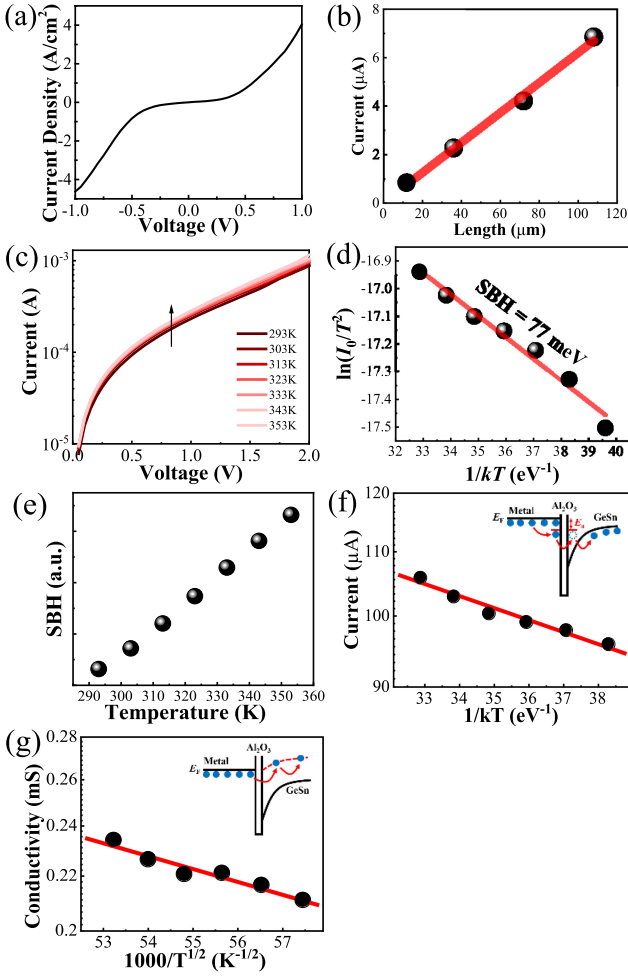
Fig. 3. (a) $J_{dark}$-$V$ characteristics for the MSM GeSnOI photodetector. (b) $I_{dark}$ for photodetectors as a function of the waveguide lengths at 1 V. (c) Temperature-dependent $I_{dark}$-$V$ characteristic for the GeSn MSM photodetector from 293 to 353 K. The arrow represents the temperature increasing from 293 to 353 K. (d) Arrhenius plot for the GeSnOI MSM photodetector as a function of $1/kT$. (e) SBH versus temperature plots for the GeSnOI MSM photodetector. (f) $I_{dark}$ for the photodetector as a function of $1/kT$. The inset in Fig. 3(f) represents the band diagram for the two-step TAT process. (g) the conductivity of the photodetectors as a function of $1000/T^{1/2}$. The inset in Fig. 3(g) represents the band diagram for the 1D-VRH process.

20 nm Ti / 50 nm TiN / 300 nm Al was performed for the metal deposition, followed by the lift-off process. The spacing distance between adjacent electrodes is 1.5 μm. The three-dimensional (3D) schematic image of the completed MSM photodetector is shown in Fig. 2(a). The top view of the scanning electron microscope (SEM) image for the GeSnOI photodetector and its zoom-in image was shown in Fig. 2(b) and the inset in Fig. 2(b), respectively. It should be noted that 1 nm of the $Al_2O_3$ layer was inserted between metal and the GeSn layer.

## III. PHOTODETECTOR CHARACTERIZATIONS

### A. Dark Current Analysis

Fig. 3(a) displays dark current density-voltage ($J_{dark}$-$V$) characterisics of the GeSn photodetector with the length of 72 μm. The symmetric $J_{dark}$ characteristics at forward and reverse bias are attributed to the equivalent conditions on both electrodes. The $J_{dark}$ for the photodetector was measured to be 4.6 A/cm² at -1 V. Fig. 3(b) displays the dark currents at 1 V for the photodetectors as a function of photodetector lengths. It should be noted that the dark current increases with the length proportionally, indicating $J_{dark}$ is consistent regardless of the photodetector lengths. In order to investigate the leakage current generation mechanism, the temperature-dependent $I_{dark}$-$V$ characteristics were performed in the temperature range from 293 to 353 K in Fig. 3(c). The Schottky Barrier Height (SBH) can be obtained by the following equations [25],

$$I_{dark} = I_0 \exp\left(\frac{qV}{nkT}\right)\left[1 - \exp\left(-\frac{qV}{kT}\right)\right], \quad (2)$$

$$I_0 = AA^*T^2 \exp\left(\frac{q\phi_b}{kT}\right), \quad (3)$$

where $I_0$ is saturation current, and $q$, $n$, $k$, and $T$ are the electron charge, ideal factor, the Boltzmann constant, and temperature, respectively. $A$, $A^*$, and $\phi_b$ are the photodetector area, the Richardson constant for GeSn, and SBH, respectively. The saturation current can be obtained by extracting the intercept of $\ln I_0$ [26]. The estimated SBH between metal and GeSn is ~77 meV, as shown in Fig. 3(d). The SBH, in general, is explained by the thermionic emission mechanism. However, the extracted SBH for the photodetector increases with temperature in Fig. 3(e), which is different from the SBH dependence on temperature caused by the thermionic emission. Such SBH change in temperature can be attributed to other leakage current mechanisms. SBH is attributed to the bandgap narrowing for GeSn. As the Sn content increases, the Ge bandgap shrinks, deforming on SBH. Also, the unintended $p$-type doping concentration increases with Sn contents, reducing SBH for the GeSn/metal Schottky contact [27]. The metal/n-GeSn contacts showed the presence of strong Fermi-level pinning effects with increasing Sn contents [28]. The high density of dislocations/defects in GeSn enhances two-step trap-assisted tunneling (TAT) or variable-range-hopping (VRG) conduction mechanisms [29]. Two-step TAT is the process where the carriers in the metal are excited thermally and tunnel via the trap states in the Schottky barrier to reach the conduction/valence bands. This tunneling mechanism is described with the equation of exp(-$E_a$/kT), where $E_a$ is the activation energy, which is the energy gap between the Fermi level and trap states in the Schottky barrier. Fig. 3(f) displays the $I_{dark}$-$1/kT$ characteristic for the photodetectors. Estimated $E_a$ is obtained to be 8 meV. The VRH mechanism is the process where the carriers in the metal fall into trap states associated with a dislocation, and they are transferred via GeSn by hopping conduction. Based on the one-dimensional (1D)-VRH model, the conductivity ($\sigma$) can be expressed by [30],

$$\sigma = \sigma_0 \exp[-(T_1/T)^{1/2}], \quad (4)$$

where $\sigma_0$ and $T_1$ are a fitting parameter of the conductance at temperature $> T_1$ and the characteristic temperature, respectively. Fig. 3(g) displays the conductivity characteristic for the photodetector as a function of $1000/T^{1/2}$. It should be noted that Fig. 3(f) and (g) show good linear fittings, indicating that
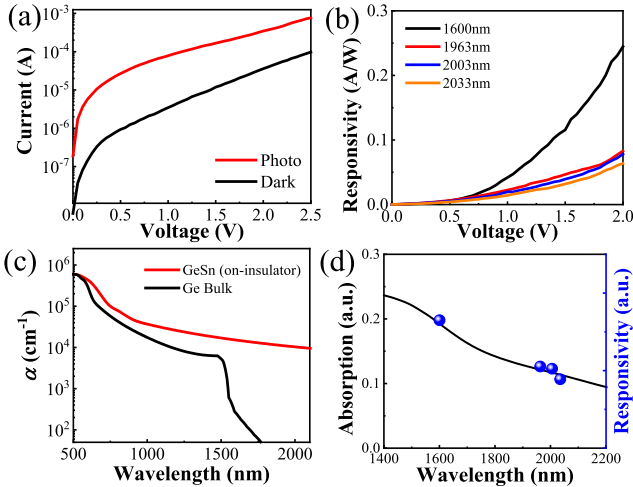
Fig. 4. (a) $I_{photo}$-$V$ characteristic of the MSM GeSnOI photodetector at 1933 nm wavelength in comparison with the $I_{dark}$-$V$ curve. (b) the measured responsivity for the photodetector at different wavelengths as a function of forward bias voltage. (c) the extracted absorption coefficient ($\alpha$) for GeSn (on-insulator) via ellipsometry in comparison with Ge bulk from [Ref. 34]. (d) the calculated absorption spectra (black line) for MSM photodetectors along with the measured responsivity (blue dots).
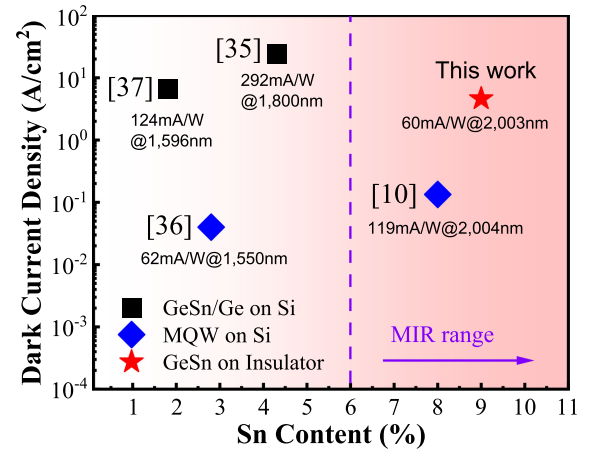


Fig. 5. Benchmarking of the dark current densities for the reported waveguide-shape GeSn photodetectors on the different platforms [10], [35]–[37]. Dark current density for each photodetector is benchmarked with respect to Sn content. Photodetectors in [10], [36] contain the GeSn MQW on Si substrate, and the photodetectors in [35], [37] contain GeSn on Ge/Si substrate. The photodetectors were cleaved for the optical measurement in [35]–[37]. The responsivities were obtained under facet illumination for [10], [35]–[37] and under surface illumination for this work.

it is difficult to tell which mechanism governs the leakage current generation. In order to reduce the leakage current for the GeSnOI photodetector, low Sn content on insulator platforms is potentially attractive due to the high-crystallinity of GeSn films [14], [31]. In addition, the advanced surface passivation can reduce the surface leakage current for the photodetectors [32], [33].

### B. Optical Characterization

The optical response was measured under normal incidence illumination. The single-mode fiber with the diameter of 10 μm was used to couple the optical power into the photodetectors. The output optical power was calibrated by using an optical power meter. The amount of the optical power arriving at the device area was obtained via the finite-difference time-domain (FDTD) method. As shown in Fig. 4(a), photocurrent ($I_{photo}$) is generated under normal incidence illumination, meaning that the photoexcited electron-hole pairs (EHPs) are generated, and they are collected by electrodes. The responsivity ($R$) can be calculated by

$$R = (I_{photo} - I_{dark})/P_{in}, \quad (5)$$

where $P_{in}$ is the output power shined on the absorption GeSn layer, excluding the shadowing of the metal contacts. In order to verify the photodetection coverage of GeSn photodetectors, various wavelength points, e.g., 1600, 1934, 2003, and 2033 nm, were selected for the optical response measurements. It is worth noting that the cut-off wavelength is beyond the 2000 nm wavelength. Fig. 4(b) represents the responsivity for the GeSnOI photodetector as a function of applied voltage. It should be noted that the responsivity increases with voltage due to the improved carrier velocity. The responsivity decreases with the increase in wavelength. The responsivity at 1600 and 2003 nm was obtained

to be 0.24 and 0.06 A/W at 2 V, respectively. The responsivity can potentially be improved by increasing the GeSn thickness or by employing the photon-trapping hole structures. Based on PL experiments, it is potentially suitable for photodetection up to the 2242 nm wavelength. In order to investigate the optical properties of the GeSnOI platform, the $n$ and $k$ values were extracted via Ellipsometry. Fig. 4(c) represents the absorption coefficient for GeSn as a function of wavelength. Compared to the absorption coefficient of Ge bulk [34], the GeSn absorption coefficient is extended beyond 2 μm. Fig. 4(d) displays the absorption spectra for the designed GeSnOI photodetectors as a function of wavelength via the FDTD method and the measured responsivity is displayed. The absorption spectra decrease with increasing wavelength, which is consistent with the responsivity.

Fig. 5 represents the benchmarking of the dark current densities for the reported GeSn waveguide-shape photodetectors [10], [35]–[37]. The bulk GeSn photodetectors on Ge/Si substrates were introduced, suffering from the high dark current densities [35], [37]. The GeSn/Ge multi-quantum-well (MQW) structures were proposed for low dark current densities due to the suppressed strain relaxation [10], [36]. In this work, the GeSnOI photodetector displays 4.6 A/cm$^2$, which is comparable to the ones for the bulk GeSn photodetectors. The responsivities with the measured wavelength are displayed in Fig. 5. The cut-off wavelength increases with the Sn contents. The GeSn/Ge MQW photodetector with the Sn content of 8% was demonstrated with the optical responsivity of ~15 and 119 mA/W at 2004 nm under surface and facet illuminations, respectively [10]. In this work, the GeSnOI photodetectors display the responsivity of 60 mA/W at 2003 nm under the surface illumination. The SiN or amorphous Si waveguides would enable the efficient photon collection for the photodetectors via the light propagation in the waveguide [38], [39]. Based on the estimated absorption coefficient of GeSn, the length of 12 μm enables the optical
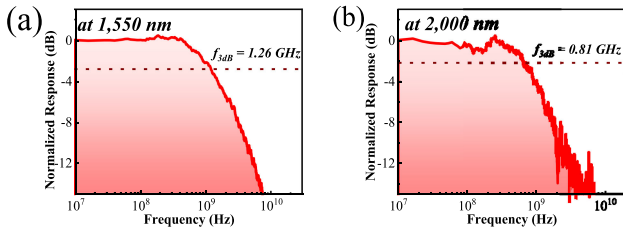
Fig. 6. Frequency response for the MSM GeSnOI photodetectors (a) at 1550 nm and (b) at 2000 nm at 0.5V.

absorption of ~100% when the light is coupled into the facet of the GeSn photodetector.

### C. Frequency Response (3 dB Bandwidth)

Fig. 6(a) and (b) displays the frequency response experiments for MSM GeSnOI photodetectors at 1550 and 2000 nm wavelength, respectively. The 3 dB bandwidth ($f_{3dB}$) is measured to be 1.26 and 0.81 GHz at 1550 and 2000 nm wavelength at 0.5 V, respectively. The trap filling effect could affect the different $f_{3dB}$ for the photodetector at 1550 and 2000 nm [40]. It should be noted that $f_{3dB}$ at 2000 nm is comparable with the one for the reported MQW GeSn waveguide photodetector at -1 V [10]. The frequency response is mainly determined by RC delay and carrier transit time [41]. The RC delay does not play a role in the photodetector with the small mesa area [35]. The capacitance for the photodetectors was obtained to be 0.5 pF. Thus, considering the load resistance of 50 Ω, $f_{3dB}$ is restricted by the carrier transit-time bandwidth ($f_T$) [42]. $f_T$ is determined by the lifetime and the transit time of photoexcited carriers. Under illumination, the photo-excited carriers are generated in the GeSn layer, and they are swept to the lateral electrodes under applied electric fields [43]. The as-grown GeSn layer is unintentionally *p*-doped due to the defects/dislocations. Thus, the GeSn layer is not fully depleted at low bias voltage range. The high $f_T$ can be observed when the saturation carrier velocity is achieved. Also, the electrode space affects the $f_{3dB}$ for photodetectors. The narrow electrode space results in high $f_T$ due to the fast carrier collection path. Lastly, the $f_{3dB}$ for the GeSn photodetector can be degraded due to the surface recombination at GeSn/Al$_2$O$_3$ [42], [44], [45]. Thus, to achieve the improved $f_{3dB}$ for the photodetectors, the optimized photodetector design and advanced surface passivation are required.

### IV. Conclusion

In this work, MSM GeSn photodetectors were demonstrated on the GeSnOI platform. The responsivity was measured to be 0.24 to 0.06 A/W at 1600 and 2003 nm wavelength, respectively. The photodetection beyond 2200 nm wavelength potentially can be measured based on the PL spectra and the extracted absorption coefficient. $J_{dark}$ for the photodetector was 4.6 A/cm$^2$. The frequency response was 1.26 and 0.81 GHz at 1550 and 2000 nm wavelengths, respectively. This GeSn/Ge interface-free GeSnOI photodetector is promising for CMOS-compatible and Si-based photonic-integrated circuits aiming to the 2 μm photodetection.

## References

[1] J. Zheng *et al.*, "Recent progress in GeSn growth and GeSn-based photonic devices," *J. Semiconductors*, vol. 39, no. 6, Jun. 2018, Art. no. 061006.

[2] P. J. Roberts *et al.*, "Ultimate low loss of hollow-core photonic crystal fibres," *Opt. Exp.*, vol. 13, no. 1, pp. 236–244, Jan. 2005.

[3] A. H. Jones, S. D. march, S. R. Bank, and J. C. Campbell, "Low-noise high-temperature AlLnAsAb/GaSb avalanche photodiodes for 2-μm applications," *Nat. Photon.*, vol. 14, no. 9, pp. 559–563, Sep. 2020.

[4] W. Cao *et al.*, "High-speed silicon modulators for the 2 μm wavelength band," *Optica*, vol. 5, no. 9, pp. 1055–1062, Sep. 2018.

[5] S. Su *et al.*, "GeSn p-i-n photodetector for all telecommunication bands detection," *Opt. Exp.*, vol. 19, no. 7, pp. 6400–6405, Mar. 2011.

[6] B. R. Conley *et al.*, "Infrared spectral response of a GeSn p-i-n photodiode on Si," in *Proc. 11th Int. Conf. Group IV Photon.*, 2014, Art. no. 14760980.

[7] H. Zhou *et al.*, "High-efficiency GeSn/Ge multiple-quantum-well photodetectors with photon-trapping microstructures operating at 2 μm," *Opt. Exp.*, vol. 28, no. 7, pp. 10280–10293, Mar. 2020.

[8] C.-H. Tan, B.-J. Huang, R. A. Soref, G. Sun, H. H. Cheng, and G.-E. Chang, "GeSn resonant-cavity-enhanced photodetectors for efficient photodetection at the 2 μm wavelength band," *Opt. Lett.*, vol. 45, no. 6, pp. 1463–1466, Mar. 2020.

[9] X. Y. Li *et al.*, "Design of Ge1-xSnx-on-Si waveguide photodetectors featuring high-speed high-sensitivity photodetection in the C- to U-bands," *Appl. Opt.*, vol. 59, no. 25, pp. 7646–7651, Sep. 2020.

[10] H. Wang, J. Zhang, G. Zhang, Y. Chen, Y.-C. Huang, and X. Gong, "High-speed and high-responsivity p-i-n waveguide photodetector at a 2 μm wavelength with a Ge$_{0.92}$Sn$_{0.08}$/Ge multiple-quantum-well active layer," *Opt. Lett.*, vol. 46, no. 9, pp. 2099–2102, May 2021.

[11] G.-E. Chang, S.-Q. Yu, J. Liu, H. H. Cheng, R. A. Soref, and G. Sun, "Achievable performance of uncooled homojunction GeSn mid-infrared photodetectors," *IEEE J. Sel. Topics Quantum Electron.*, vol. 28, no. 2, Mar. 2021, Art. no. 3800611, doi: 10.1109/JSTQE.2021.3065204.

[12] R. Loo *et al.*, "Epitaxial GeSn: Impact of process conditions on material quality," *Semicond. Sci. Technol.*, vol. 33, no. 11, Oct. 2018, Art. no. 114010.

[13] W. Dou *et al.*, "Investigation of GeSn strain relaxation and spontaneous composition gradient for low-defect and high-Sn alloy growth," *Sci. Rep.*, vol. 8, no. 1, pp. 5640, Apr. 2018.

[14] K. Ye *et al.*, "Absorption coefficients of GeSn extracted from PIN photodetector response," *Solid-State Electron.*, vol. 110, pp. 71–75, Aug. 2015.

[15] H. Tran *et al.*, "Si-based GeSn photodetectors toward mid-infrared imaging applications," *ACS Photon.*, vol. 6, no. 11, pp. 2807–2815, Oct. 2019.

[16] A. Elbaz *et al.*, "Ultra-low-threshold continuous-wave and pulsed lasing in tensile-strained GeSn alloys," *Nat. Phot.*, vol. 14, no. 6, pp. 375–382, Jun. 2020.

[17] A. Elbaz *et al.*, "Reduced lasing thresholds in GeSn microdisk cavities with defect management of the optically active region," *ACS Photon.*, vol. 7, no. 10, pp. 2713–2722, Sep. 2020.

[18] D. Lei *et al.*, "GeSn-on-insulator substrate formed by direct wafer bonding," *Appl. Phys. Lett.*, vol. 109, no. 2, Jul. 2016, Art. no. 022106.

[19] S. Gupta *et al.*, "Highly selective dry etching of germanium over germanium-tin (Ge$_{1-x}$Sn$_x$): A novel route for Ge$_{1-x}$Sn$_x$ nanostructure fabrication," *Nano Lett.*, vol. 13, no. 8, pp. 3783–3790, Aug. 2013.

[20] S. A. Ghetmiri *et al.*, "Shortwave-infrared photoluminescence from Ge$_{1-x}$Sn$_x$ thin films on silicon," *J. Vac. Sci. Technol. B*, vol. 32, no. 6, Nov. 2014, Art. no. 060601.

[21] A. Gassenq *et al.*, "Raman spectral shift versus strain and composition in GeSn layers with 6%-15% Sn content," *Appl. Phys. Lett.*, vol. 110, no. 11, Mar. 2017, Art. no. 112101.

[22] J. Aubin *et al.*, "Growth and structural properties of step-graded, high Sn content GeSn layers on Ge," *Semicond. Sci. Tech.*, vol. 32 no. 9, Aug. 2017, Art. no. 094006.

[23] H. V. Stanchu *et al.*, "Quantitative correlation study of dislocation generation, strain relief, and Sn outdiffusion in thermally annealed GeSn epilayers," *Cryst. Growth Des.*, vol. 21, no. 3, pp. 1666–1673, Jan. 2021.

[24] Y. Zhou *et al.*, "Alleviation of Fermi-level pinning effect on metal/germanium interface by insertion of an ultrathin aluminum oxide," *Appl. Phys. Lett.*, vol. 93, no. 20, Nov. 2008, Art. no. 202105.

[25] T. Asar and S. Özçelik, "Barrier enhancement of Ge MSM IR photodetector with Ge layer optimization," *Superlattices Microstructures*, vol. 88, pp. 685–694, Dec. 2015.

[26] H. Zhou *et al.*, "Surface plasmon enhanced GeSn photodetectors operating at 2 μm," *Opt. Exp.*, vol. 29 no. 6, pp. 8498–8509, Mar. 2021.

[27] C. Schilte-Braucks *et al.*, "Schottky barrier tuning via dopant segregation in NiGeSn-GeSn contacts," *J. Appl. Phys.*, vol. 121, no. 20, May 2017, Art. no. 205705.

[28] Y. Chuang, C.-Y. Liu, H.-S. Kao, K.-Y. Tien, G.-L. Luo, and J.-Y. Li, "Schottky barrier height modulation of metal/n-GeSn contacts featuring low contact resistivity by in situ chemical vapor deposition doping and nigesn alloy formation," *ACS Appl. Electron. Mater.*, vol. 3, no. 3, pp. 1334–1340, Mar. 2021.

[29] H. Fu *et al.*, "A comparative study on the electrical properties of vertical (201) and (010) $\beta$-Ga$_2$O$_3$ Schottky barrier diodes on EFG single-crystal substrates," *IEEE Trans. Electron Devices*, vol. 65, no. 8, pp. 3507–3513, Jun. 2018.

[30] E. J. Miller, E. T. Yu, P. Waltereit, and J. S. Speck, "Analysis of reverse-bias leakage current mechanisms in GaN grown by molecular-beam epitaxy," *Appl. Phys. Lett.*, vol. 84, no. 4, pp. 535–537, Jan. 2004.

[31] B. Son, L. Zhang, Y. Jung, H. Zhou, D. Nam, and C. S. Tan, "Systematic study on photoexcited carrier dynamics related to defects in GeSn films with low Sn content at room temperature," *Semicond. Sci. Tech.*, vol. 36, no. 12, Nov. 2021, Art. no. 125018.

[32] Y. Dong *et al.*, "Suppression of dark current in germanium-tin on silicon p-i-n photodiode by a silicon surface passivation technique," *Opt. Exp.*, vol. 23, no. 14, pp. 18611–18619, Jul. 2015.

[33] Y.-C. Fang, K.-Y. Chen, C.-H. Hsieh, C.-C. Su, and Y.-H. Wu, "N-MOSFETs formed on solid phase epitaxially grown GeSn film with passivation by oxygen plasma featuring high mobility," *ACS Appl. Mater. Interfaces*, vol. 7, no. 48, pp. 26374–26380, Dec. 2015.

[34] D. E. Aspnes and A. A. Studna, "Dielectric functions and optical parameters of Si, Ge, GaP, GaSb, InP, InAs, and InSb from 1.5 to 6.0 eV," *Phys. Rev.* vol. 27, no. 2, pp. 985–1009, Jan. 1983.

[35] C.-H. Tsai, K.-C. Lin, C.-Y. Cheng, K.-C. Lee, H. H. Cheng, and G.-E. Chang, "GeSn lateral p-i-n waveguide photodetectors for mid-infrared integrated photonics," *Opt. Lett.*, vol. 46, no. 4, pp. 864–867, Feb. 2021.

[36] Y.-H. Huang, G.-E. Chang, H. Li, and H. H. Cheng, "Sn-based waveguide p-i-n photodetector with strained GeSn/Ge multiple-quantum-well active layer," *Opt. Lett.*, vol. 42 no. 9, pp. 1652–1655, May 2017.

[37] Y.-H. Peng, H. H. Cheng, V. I. Mashanov, and G.-E. Chang, "GeSn p-i-n waveguide photodetectors on silicon substrates," *Appl. Phys. Lett.*, vol. 105, no. 23, Dec. 2014, Art. no. 231109.

[38] J. Kang, S. Takago, and M. Takenaka, "Ge photodetector monolithically integrated with amorphous Si waveguide on wafer-bonded Ge-on-insulator substrate," *Opt. Exp.*, vol. 26 no. 23, pp. 30546–30555, Nov. 2018.

[39] S. Yanikgonul *et al.*, "Integrated avalanche photodetectors for visible light," *Nat. Commun.*, vol. 12, no. 1, pp. 1834, Mar. 2021, Art. no. 1834.

[40] A. Uleckas *et al.*, "Analysis of auger recombination characteristics in high resistivity Si and Ge," *Solid State Phenomena*, vol. 178-179, pp. 427–432, 2011.

[41] B. Son, H. Zhou, Y. Lin, K. H. Lee, and C. S. Tan, "Gourd-shaped hole array germanium (Ge)-on-insulator photodiodes with improved responsivity and specific detectivity at 1,550 nm," *Opt. Exp.*, vol. 29 no. 11, pp. 16520–16533, May 2021.

[42] W. Wang *et al.*, "High-performance GeSn photodetector and fin field-effect transistor (FinFET) on an advanced GeSn-on-insulator platform," *Opt. Exp.*, vol. 26 no. 8, pp. 10305–10314, Apr. 2018.

[43] G. Dushaq, A. Nayfeh, and M. Rasras, "Metal-germanium-metal photodetector grown on silicon using low temperature RF-PECVD," *Opt. Exp.*, vol. 25 no. 25, pp. 32110–32119, Dec. 2017.

[44] S. Ke *et al.*, "Voltage sharing effect and interface state calculation of a wafer-bonding Ge/Si avalanche photodiode with an interfacial GeO$_2$ insulator layer," *Opt. Exp.*, vol. 23 no. 3, pp. 1943–1952, Feb. 2016.

[45] B. Son, Y. Lin, K. H. Lee, Y. Wang, S. Wu, and C. S. Tan, "High speed and ultra-low dark current Ge vertical p-i-n photodetectors on an oxygen-annealed Ge-on-insulator platform with GeO$_x$ surface passivation," *Opt. Exp.*, vol. 28, no. 16, pp. 23978–23990, Aug. 2020.